

RESEARCH ARTICLE

10.1002/2013JB010710

This is a companion paper to *Platt et al.* [2014], doi:10.1002/2013JB010710.

Key Points:

- Rapid shear in a fluid-saturated gouge material is unstable
- A linear stability analysis allows us to predict a localized zone thickness
- Typical localized zone thicknesses are 5–40 microns, in line with observations

Correspondence to:

J. D. Platt,
jplatt@seas.harvard.edu

Citation:

Rice J. R., J. W. Rudnicki, and J. D. Platt (2014), Stability and localization of rapid shear in fluid-saturated fault gouge: 1. Linearized stability analysis, *J. Geophys. Res. Solid Earth*, 119, 4311–4333, doi:10.1002/2013JB010710.

Received 25 SEP 2013

Accepted 17 APR 2014

Accepted article online 23 APR 2014

Published online 19 MAY 2014

Stability and localization of rapid shear in fluid-saturated fault gouge: 1. Linearized stability analysis

James R. Rice^{1,2}, John W. Rudnicki^{3,4}, and John D. Platt¹

¹School of Engineering and Applied Sciences, Harvard University, Cambridge, Massachusetts, USA, ²Department of Earth and Planetary Sciences, Harvard University, Cambridge, Massachusetts, USA, ³Department of Mechanical Engineering, Northwestern University, Evanston, Illinois, USA, ⁴Department of Civil and Environmental Engineering, Northwestern University, Evanston, Illinois, USA

Abstract Field observations of major earthquake fault zones show that shear deformation is often confined to principal slipping zones that may be of order 1–100 μm wide, located within a broader gouge layer of order 10–100 mm wide. This paper examines the possibility that the extreme strain localization observed may be due to the coupling of shear heating, thermal pressurization, and diffusion. In the absence of a stabilizing mechanism shear deformation in a continuum analysis will collapse to an infinitesimally thin zone. Two possible stabilizing mechanisms, studied in this paper, are rate-strengthening friction and dilatancy. For rate-strengthening friction alone, a linear stability analysis shows that uniform shear of a gouge layer is unstable for perturbations exceeding a critical wavelength. Using this critical wavelength we predict a width for the localized zone as a function of the gouge properties. Taking representative parameters for fault gouge at typical centroidal depths of crustal seismogenic zones, we predict localized zones of order 5–40 μm wide, roughly consistent with field and experimental observations. For dilatancy alone, linearized strain rate perturbations with a sufficiently large wavelength will undergo transient exponential growth before decaying back to uniform shear. The total perturbation strain accumulated during this transient strain rate localization is shown to be largely controlled by a single dimensionless parameter E , which is a measure of the dilatancy of the gouge material due to an increase in strain rate.

1. Introduction

Detailed examinations of fault zones have shown a hierarchical structure, with a fault core composed of ultracataclasite and fault gouge sitting within a broader damage zone. Further investigation reveals a zone of highly localized shear on the order of 10–300 μm wide nested within the fault core [Heermance et al., 2003; Chester et al., 2003; De Paola et al., 2008]. This localized shear zone is interpreted as the principal slip surface of the fault. What determines the width of this zone? Extreme localization is readily understandable in a fluid-saturated fault gouge undergoing thermal pressurization during shear. In this paper and the companion paper [Platt et al., 2014] we study how two localization limiting mechanisms could combine with thermal pressurization and hydrothermal diffusion to set the width of the localized shear zone during rapid shear. The first limiting mechanism is frictional rate strengthening. The friction coefficient varies with the rate of shearing in a manner suggested by laboratory experiments, with strengthening observed at higher temperatures or higher-clay fractions. Such rate-strengthening friction is appropriate in stable regions of faults where rupture cannot nucleate but can propagate through, or in initially unstable regions that have been driven to high temperatures by shear heating. The second limiting mechanism is dilatancy. The gouge porosity, and hence pore fluid volume, increases with shear strain rate, reducing the pore pressure. When this occurs faster than fluid diffusion into the newly expanded pore space, dilatancy will have a strengthening effect. In the absence of a limiting mechanism the shearing will collapse to a zone of zero width in a continuum model, as noted in Rice [2006]. In this paper we present a linear stability analysis of these two mechanisms separately. For frictional rate strengthening alone the solution for homogeneous deformation of the gouge presented in Lachenbruch [1980] is unstable for gouge layer thicknesses exceeding a critical value. This critical thickness is interpreted as the localization thickness during rapid shear. For dilatancy alone the linear stability analysis

predicts intense transient strain rate localization, followed by a return to uniform shear of the gouge layer at large slips. We show that except for very small wavelengths, the total accumulated strain during this transient localization is controlled by a single dimensionless parameter representing the efficiency of dilatant strengthening.

The companion paper [Platt *et al.*, 2014] presents full numerical simulations that complement the linear stability predictions of this paper. These simulations show that for both stabilizing mechanisms the final localized zone thickness is almost independent of the initial thickness of the gouge layer and is controlled by the physical properties of the gouge. The influence of strain rate localization on shear strength evolution is also studied, and we observe dramatic weakening associated with the onset of localization caused by the focusing of frictional heating into a narrower zone.

1.1. Field Observations of Strain Localization

Chester and Chester [1998] studied the structure of the Punchbowl fault, an inactive branch of the San Andreas Fault system thought to have accommodated 44 km of slip [Chester *et al.*, 2004], at a depth of ~ 3 –4 km [Polissar *et al.*, 2011]. They observed a continuous ultracataclasite layer 0.15–0.55 m wide, surrounded by a much broader damage zone ~ 15 m wide. Within this ultracataclasite layer there runs a single continuous fracture surface, which Chester and Chester [1998] called the principal fracture surface, parallel to the direction of shear. Other fracture surfaces exist but are < 1 m in length and are truncated by the principal fracture surface. These fracture surfaces are thought to represent strain localization within the ultracataclasite layer, and the principal fracture surface is identified as the principal slip surface for the Punchbowl fault. Subsequent studies of a thin section sample under cross-polarized light showed that the majority of the shearing had been accommodated within in a zone just 100–300 μm wide [Chester *et al.*, 2003] (see the thin section from their work reproduced in Rice [2006, Figure 1b]). The concurrent work of Heermance *et al.* [2003] also showed 100 micron-scale strain localization and will be discussed further below.

In another study De Paola *et al.* [2008] analyzed a series of normal faults in the Northern Apennines, hosted in dolostone and anhydrite rocks. On small displacement faults, with a slip of < 10 m, they observed a cataclasite fault core a few centimeters thick. Within this gouge layer zones of intense shear strain localization are observed, ranging in width from a few to tens of microns, running parallel to the fault core boundary. De Paola *et al.* [2008] also studied a larger displacement fault, with a slip of > 100 m. In this case the fault core was much broader, 5–6 m wide, and contained multiple principal slip surfaces. Associated with each principal slip surface was a layer of very fine grained cataclasites 2–3 mm wide, and within each of these layers they observed a zone of localized shear ~ 10 μm wide. These observations appear to show that in the region studied in De Paola *et al.* [2008], although the width of the fault core and surrounding damage zone increases with fault displacement, the localized shear zones observed are consistently ~ 1 –10 μm wide.

Not all field observations showed micron-scale strain localization. Boullier *et al.* [2009] analyzed the microstructural distribution in two borehole samples taken from depths of 1111 m and 1136 m on the Chelungpu fault after the M_w 7.6 Chi-Chi earthquake in 1999. In both samples they interpreted the principal slip surface to be an isotropic gouge layer 3–20 mm wide with no evidence of submillimeter-scale localized shear structures. Heermance *et al.* [2003] also analyzed the principal slip surface of the Chelungpu fault using a combination of borehole drilling and outcrops. They found evidence of extreme strain localization in the northern region of the fault, down to a width of approximately 50–300 μm , and much more diffuse deformation in the southern region. Noting that the location of distributed shear in Boullier *et al.* [2009] is near the location of micron-scale localization in Heermance *et al.* [2003] it appears that extreme strain localization does not occur in every seismic event, and there may be significant spatial variation in the localized zone thickness. For completeness we also mention one final observation of millimeter-scale localization to supplement the centimeter-scale and micron-scale structures discussed above. Wibberley and Shimamoto [2003] identified a “central slip zone” on the Median Tectonic Line fault with a nominal thickness of 3 mm (C. A. Wibberley, private communication, 2003), although no measurements were made to look for finer-scale structures within this zone.

It should be noted that there is no definitive proof that the shear zones described in this subsection are formed coseismically, though highly localized shear is commonly used as an indicator of seismic deformation.

1.2. Localization in High-Velocity Friction Experiments

Velocity-stepping experiments first presented in *Dieterich* [1979] have led to a much clearer understanding of friction, and the frictional response to velocity changes, at slip rates of $\sim 1\text{--}10\ \mu\text{m/s}$. However, the picture at seismic slip rates is much less clear with complicated thermal and hydraulic processes obscuring the purely frictional response. Rotary shear devices have been used in recent years to investigate this high-velocity regime for rock-rock friction and gouge materials [*Tsutsumi and Shimamoto*, 1997]. In a typical experiment, for example, *Brantut et al.* [2008], *Kitajima et al.* [2010], *Reches and Lockner* [2010], *Smith et al.* [2013], and many additional studies, a gouge layer around 1 mm wide is confined between two cylindrical blocks, one rotating and one stationary, leading to rapid shearing of the gouge.

Kitajima et al. [2010] performed rotary shear experiments on a fluid-saturated gouge composed of disaggregated ultracataclasite from the Punchbowl fault. The resulting microstructures were analyzed under plane-polarized and cross-polarized light by cutting thin sections through the axis of the cylinder, creating a radial cross section of the gouge material. Four distinct microstructural units were identified, and the formation of the different units was correlated with different slip and slip rate conditions. At slip rates of $\sim 1\ \text{m/s}$ they observed two distinct microstructural units, one a less compacted gouge with a random fabric, the other a zone of extremely fine grained material with a very strong foliation that is interpreted as a region of intense strain localization. The width of this localized zone is typically $\sim 100\ \mu\text{m}$. However, the distinct banded nature of the zone of highly localized shear may indicate multiple slipping zones each much thinner than the total width of the localized zone. *Kitajima et al.* [2010] linked the onset of strain localization with the observed dynamic weakening, an observation in agreement with the results presented in the companion paper [*Platt et al.*, 2014].

A similar set of rotary shear experiments was presented in *Brantut et al.* [2008] using gouge taken from the Median Tectonic Line, southwest Japan. Optical microscopy showed a thin, darker zone $\sim 1\text{--}10\ \mu\text{m}$ wide, which due to a lack of other indications of deformation in the gouge layer was identified as the main slipping zone of the experiment. Other high-velocity friction experiments [*Boutareaud et al.*, 2008; *Mizoguchi et al.*, 2009] have also shown evidence of micron-scale strain localization.

It should be noted that micron-scale strain localization also occurs in rotary shear experiments performed at slip rates of $\sim 10\ \mu\text{m/s}$ [*Yund et al.*, 1990; *Beeler et al.*, 1996], and the model presented here cannot explain these observations.

1.3. Influence on Rupture Properties

Previous studies of thermally driven weakening mechanisms have shown that the width of the deforming zone is a key parameter. Narrow deforming zones concentrate the frictional heating leading to large temperature rises, and thus more rapid weakening. This can be seen in the solution of *Lachenbruch* [1980] for uniform shear of a gouge layer undergoing thermal pressurization, where the slip-weakening distance scales linearly with the width of the deforming zone. Very thin zones require only small slips to cause dynamic weakening. This may explain why the gouge layer width plays a significant role in determining the rupture propagation mode in the calculations performed in *Noda et al.* [2009], which showed a transition from crack-like ruptures through growing slip pulses to arresting slip pulses as the gouge layer thickness was increased. Thinner layers will experience more weakening and thus are more likely to propagate as an accelerating crack-like rupture. Extending the thermal pressurization model in a different direction, *Rempel and Rice* [2006] studied the temperature rise expected for a uniformly sheared, fluid-saturated gouge layer. They found that for a fixed amount of slip, thinner shear zones will experience larger temperature rises. Thus, the deforming zone thickness may determine if melting occurs, or if other temperature controlled dynamic weakening mechanisms such as thermal decomposition are activated. A final example of the importance of the deforming zone thickness are the solutions for a steadily propagating slip pulse presented in *Garagash* [2012]. In these results the total slip in the event scales linearly with the deforming zone thickness, and the slip duration scales as the square of the deforming zone thickness.

2. Model Derivation

Figure 1 shows an idealized one-dimensional model for deformation of a fluid-saturated gouge material. The layer represents a gouge zone inherited from previous stable or seismic slip. In this model the only nonzero velocity component, $u(y, t)$, is parallel to the fault zone and depends only on the time since the onset

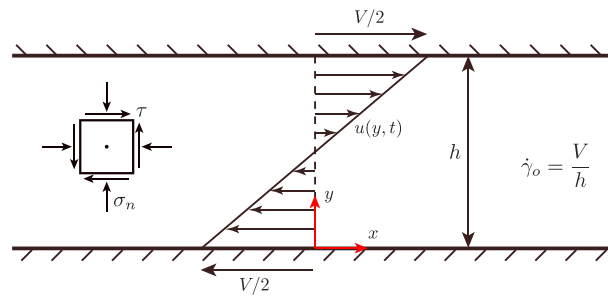


Figure 1. A fault zone idealized as a gouge layer of thickness h subjected to homogeneous shear strain rate $\dot{\gamma}_o$. The stresses in the layer are a constant normal stress σ_n , a shear stress τ , and whatever other normal stresses in the x and z directions needed to maintain zero normal strain in these directions.

of shear, t , and the coordinate perpendicular to the direction of slip, y . The stresses in the deforming zone are the shear stress τ , a constant compressive normal stress σ_n in the y direction, and whatever other normal stresses are required to meet the constraints of zero straining in the other directions.

We do not intend to model a specific fault, and our results are valid for any fluid-saturated gouge material with a rate-strengthening friction law. Seismic shear in rate-strengthening materials is expected to occur when a rupture that nucleated elsewhere propagates into a

stably creeping region of a fault, or when a fault that can nucleate earthquakes is heated to temperatures associated with rate-strengthening friction [Blanpied et al., 1998; Boettcher et al., 2007].

2.1. Mechanical Equilibrium

Rice [2006] hypothesized that inertial effects within the gouge will be negligible since even very large accelerations contribute a small amount to the change of stress over the small distances, on the order of a few tens of millimeters, over which thermal and fluid diffusion is important. This means that the deformation process can be approximated as quasi-static, and the stresses within the layer satisfy

$$\frac{\partial \tau}{\partial y} = 0 \quad , \quad \frac{\partial \sigma_n}{\partial y} = 0. \tag{1}$$

The quasi-static approximation means that the shear and normal stress do not depend on y and are at most a function of t . In the companion paper to this study we further analyze the small inertial effects and investigate under what conditions they may become important.

2.2. Gouge Friction

The shear stress is taken to be the product of a friction coefficient f and the Terzaghi effective stress

$$\tau = f(\sigma_n - p), \tag{2}$$

where $p = p(y, t)$ is the pore pressure. Many studies of thermally driven weakening mechanisms assume that the friction coefficient is constant. When constant friction and mechanical equilibrium are assumed, and dilatancy is neglected, only two forms of deformation are possible, homogeneous shear in the gouge material or slip on the plane of maximum pore pressure [Rice, 2006]. However, when the friction coefficient is allowed to vary, a finite thickness shear zone can exist, with regions of large pore pressure balanced by larger-friction coefficients. In this paper we consider a friction coefficient that is a function of the strain rate alone.

$$f = f(\dot{\gamma}) \quad , \quad \dot{\gamma} = \frac{\partial u}{\partial y}. \tag{3}$$

The analysis in this paper requires only the linearization of the friction law around the uniform strain rate $\dot{\gamma}_o$,

$$f(\dot{\gamma}) = f_o + \frac{a-b}{\dot{\gamma}_o}(\dot{\gamma} - \dot{\gamma}_o), \tag{4}$$

where we have defined

$$f_o = f(\dot{\gamma}_o) \quad , \quad (a-b) = \dot{\gamma}_o \left. \frac{df}{d\dot{\gamma}} \right|_{\dot{\gamma}=\dot{\gamma}_o} \tag{5}$$

We consider a rate-strengthening material so $(a-b) > 0$. The form of these coefficients is chosen so that $(a-b)$ is equivalent to the typical rate-and-state friction parameter when one writes

$$f = f_o + (a-b) \log(\dot{\gamma}/\dot{\gamma}_o) \tag{6}$$

for shearing at steady state. However, the results in this paper are valid for any friction law that depends on strain rate alone. We ignore the state evolution effects accompanying changes in shear rate, since there is no presently accepted way of describing these effects of distributed shear in gouge. For regions of rate-weakening friction a fuller description that includes a dependence on state and a procedure to limit localization would be needed. The inclusion of the direct effect, meaning that any increase in strain rate leads to a transient increase in the friction coefficient, may prevent localization from evolving to an infinitesimally narrow zone.

2.3. Conservation of Energy

Conservation of energy can be expressed as

$$\tau \dot{\gamma} = \rho c \frac{\partial T}{\partial t} + \frac{\partial q_h}{\partial y} \quad (7)$$

where T is the temperature, c is the specific heat, ρ is the density in the reference state, and q_h is the heat flux. This expression neglects generally small additional terms due to the work of the normal stress and pore pressure, and internal energy transfer due to flow of the fluid, a common assumption justified in *Mase and Smith* [1985, 1987] for representative permeabilities of fault gouges. The heat flux is related to the temperature gradient by Fourier's law

$$q_h = -K \frac{\partial T}{\partial y} \quad (8)$$

where K is the thermal conductivity. Substituting (8) into (7) and simplifying we arrive at

$$\frac{\partial T}{\partial t} = \frac{\tau \dot{\gamma}}{\rho c} + \alpha_{th} \frac{\partial^2 T}{\partial y^2} \quad (9)$$

where $\alpha_{th} = K/\rho c$ is the thermal diffusivity. When combining equations (8) and (9) we have assumed that the thermal conductivity is insensitive to temperature and porosity changes.

2.4. Conservation of Pore Fluid Mass

Conservation of pore fluid mass can be expressed as

$$\frac{\partial m}{\partial t} + \frac{\partial q_f}{\partial y} = 0 \quad (10)$$

where m is the fluid mass per unit volume of porous medium with that volume as measured in a reference state and q_f is the pore fluid mass flux. According to Darcy's law, this mass flux is proportional to the negative of the pore pressure gradient,

$$q_f = -\frac{\rho_f k}{\eta_f} \frac{\partial p}{\partial y} \quad (11)$$

where k is the intrinsic permeability and ρ_f and η_f are the density and viscosity of pore fluid, respectively. Writing $m = \rho_f n$, where n is the porosity, and differentiating this product yields

$$\frac{\partial m}{\partial t} = n \frac{\partial \rho_f}{\partial t} + \rho_f \left(\frac{\partial n^{el}}{\partial t} + \frac{\partial n^{pl}}{\partial t} \right) \quad (12)$$

Here the rate of change of the porosity has been written as the sum of elastic and inelastic or plastic contributions from dilatancy, as in the *Segall and Rice* [1995] formulation. We later explain a possible reinterpretation of the symbols n^{el} and n^{pl} in a manner consistent with critical state soil mechanics [*Schofield and Wroth*, 1968; *Muir-Wood*, 1990] which may be more appropriate for sustained shearing (rather than nucleation of instability as considered in *Segall and Rice* [1995]). Variations in the elastic porosity with pore pressure and temperature can be accounted for by setting

$$\frac{1}{n} \frac{\partial n^{el}}{\partial t} = \beta_n \frac{\partial p}{\partial t} + \lambda_n \frac{\partial T}{\partial t} \quad (13)$$

where β_n and λ_n are the compressibility and the thermal expansivity of the pore volume, respectively. These can be expressed in terms of coefficients for porothermoelasticity [*McTigue*, 1986; *Coussy*, 1995] evaluated for constant normal stress perpendicular to the fault zone ($\sigma_n = \text{const}$) and zero normal strains in the

plane of the fault zone [see Rice, 2006]. In a similar fashion the rate of change of the fluid density ρ_f can be expressed as

$$\frac{1}{\rho_f} \frac{\partial \rho_f}{\partial t} = \beta_f \frac{\partial p}{\partial t} - \lambda_f \frac{\partial T}{\partial t} \quad (14)$$

where β_f and λ_f are the compressibility and thermal expansivity of the pore fluid, respectively. Combining equations (10)–(14) we arrive at

$$\frac{\partial p}{\partial t} = \Lambda \frac{\partial T}{\partial t} - \frac{1}{\beta} \frac{\partial n^{\text{pl}}}{\partial t} + \alpha_{\text{hy}} \frac{\partial^2 p}{\partial y^2} \quad (15)$$

where

$$\beta \equiv n(\beta_f + \beta_n) \quad , \quad \Lambda \equiv \frac{\lambda_f - \lambda_n}{\beta_f + \beta_n} \quad (16)$$

Here β is an elastic storage coefficient and Λ is the ratio of pore pressure change to temperature change during undrained, adiabatic elastic deformation. The hydraulic diffusivity is defined as

$$\alpha_{\text{hy}} = k/[n_f n(\beta_f + \beta_n)] \quad (17)$$

and is assumed to be constant. The first term on the right-hand side of equation (15) models thermal pressurization, the second term models pore pressure drops due to inelastic porosity increases, and the final term represents hydraulic diffusion.

Equations equivalent to (9) and (15) have been used by *Garagash and Rudnicki* [2003] and *Segall and Rice* [1995] with $\partial^2 p / \partial y^2$ and $\partial^2 T / \partial y^2$ approximated by the difference between local and remote values of p and T divided by a characteristic length squared. This form is appropriate for the single degree of freedom (spring slider) model considered in those papers but is too severe an idealization for continuum deformation.

2.5. Gouge Dilatancy

In this paper we assume that all of the inelastic porosity change is due to dilatancy, although other mechanisms also exist, with one possible example being thermal decomposition [*Sulem and Famin*, 2009]. We assume that the gouge is sufficiently sheared that all porosity changes are due to changes in strain rate, allowing us to write $n^{\text{pl}} = n^{\text{pl}}(\dot{\gamma})$. As with the friction law, the analysis in this paper requires only the linearized form,

$$n^{\text{pl}}(\dot{\gamma}) = n_o^{\text{pl}} + \varepsilon \frac{\dot{\gamma} - \dot{\gamma}_o}{\dot{\gamma}_o}, \quad (18)$$

where we define

$$n_o^{\text{pl}} = n^{\text{pl}}(\dot{\gamma}_o) \quad , \quad \varepsilon = \dot{\gamma}_o \left. \frac{dn^{\text{pl}}}{d\dot{\gamma}} \right|_{\dot{\gamma}=\dot{\gamma}_o} \quad (19)$$

Here n_o^{pl} is the plastic porosity at the uniform strain rate $\dot{\gamma}_o$ and ε is a measure of the strength of dilatancy in the gouge material, with a larger value of ε leading to more dilation. The forms of the coefficients are chosen to agree with the steady state form for shear dilatancy at low strain rates introduced by *Segall and Rice* [1995] and based on experiments in *Marone et al.* [1990]. Note that the dilatancy rate vanishes for constant strain rate.

2.6. Critical State Reinterpretation

In the classical critical state formulation for sustained shear, rate effects are ignored and the porosity is taken to be a function of effective normal stress (which we may generalize to be a function of effective stress and, weakly, temperature). We reinterpret the symbol n^{el} as

$$n^{\text{el}} = n^{\text{cs}}(\sigma_n - p, T) \quad (20)$$

where the superscript cs denotes critical state and, in our case, σ_n is constant. That is, we represent the porosity as the sum of the rate-independent critical state form (20) and take n^{pl} as above in equations (18) and (19) to represent the actual rate effects neglected in the standard critical state formulations. Thus,

Table 1. Representative Parameters Modeling a Centroidal Depth of 7 km^a

Parameter	Intact Material, Nominal Values	Intact Material, Path-Averaged Values	Damaged Material, Nominal Values	Damaged Material, Path-Averaged Values
α_{th} , mm ² /s	0.7	0.66	0.7	0.54
ρc , MPa/K	2.7	2.7	2.7	2.7
Λ , MPa/K	0.93	0.89	0.31	0.30
α_{hy} , mm ² /s	0.86	2.05	3.52	6.71
β , $\times 10^{-10}$ Pa ⁻¹	0.52	0.55	1.26	2.97
ϵ	1.7×10^{-4}	1.7×10^{-4}	1.7×10^{-4}	1.7×10^{-4}
$\sigma_n - p_a$, MPa	126	126	126	126
ρ , kg/m ³	2800	2800	2800	2800

^aThermal and hydraulic properties are taken from *Rempel and Rice* [2006, Table 1], based on [*Rice*, 2006, Tables 1–3] and the procedures in *Rice* [2006] to take account of (1) damage to the fault zone material at the onset of shearing, due to concentrated stresses near the tip of a propagating rupture front, and (2) variations of properties with pressure and temperature (for the path-averaged values). To model the damaged gouge, permeability is increased by a factor of 10, and the drained compressibility by a factor of 2. The path-averaged values roughly account for parameter variations with pore pressure p and temperature T ; a p - T path is calculated based on the nominal parameters, and new parameter values are chosen as averages of parameter values along that path. The ambient effective stress is calculated using an effective stress gradient of 18 MPa/km. The value of ϵ is taken from *Segall and Rice* [1995] and is found by fitting to the low strain rate experiments performed by *Marone et al.* [1990].

β_n and λ_n are redefined by equation (13) above, now with n^{el} replaced by n^{cs} , with σ_n constant. They are now interpreted as coefficients expressing rate-independent changes of porosity linearized about the critical state.

We expect the (small) thermal expansion effect to be little changed, although now β_n is expected to be larger because the change of porosity n with effective stress at the critical state (defining $-\beta_n$) is comparable in magnitude to the change of n with effective stress during one-dimensional consolidation. The latter compressibility is typically several times larger than the compressibility for elastic response (say by unloading from one-dimensional consolidation), which is the basis for estimates of β_n in *Segall and Rice* [1995] and *Rice* [2006].

3. Parameter Values

The hydraulic parameters of the problem are poorly constrained and depend strongly on the stress state, pore pressure, temperature, and amount of damage that develops during initial shear of the fault gouge. To account approximately for these complications we use the parameters in *Rempel and Rice* [2006, Table 1], which are based on *Rice* [2006, Tables 1–3] and the procedures in *Rice* [2006] to account for damage and variations of properties with pressure and temperature.

The large stresses near the tip of a dynamically propagating rupture may alter the gouge through processes such as comminution and opening of cemented microcracks. To model this damage *Rice* [2006] made the somewhat arbitrary choices to increase the permeability by a factor of 10 and the drained compressibility by a factor of 2 relative to their laboratory values at a given stress, pore pressure, and temperature. This leads to parameter sets modeling an intact and damaged material.

Pore fluid properties, and thus parameters such as α_{hy} and Λ that depend on the fluid properties, will change with pore pressure and temperature. The simplest choice to account for these changes is to evaluate all properties at the ambient pore pressure and temperature conditions. We call parameter sets created using this choice the nominal parameters. Another approach suggested in *Rice* [2006] is to average the parameters over the p - T path anticipated from calculations based on the nominal parameter values. Parameter sets that use this method are called path-averaged parameters.

These methods lead to the four parameter sets, nominal and path-averaged parameters for an intact and damaged material, summarized in Table 1. All four parameter sets are intended to model a depth of 7 km, a typical centroidal depth for a crustal seismogenic zone.

The final parameter in the pore pressure equation is ϵ , which models the inelastic porosity change associated with a change in strain rate. We choose $\epsilon = 1.7 \times 10^{-4}$, which is the value *Segall and Rice* [1995] found

Table 2. Representative Parameters Modeling a Depth of 1 km, Taken From *Platt et al.* [2014]^a

Parameter	Intact Material	Damaged Material
α_{th} , mm ² /s	0.7	0.7
ρc , MPa/K	2.7	2.7
Λ , MPa/K	0.22	0.068
α_{hy} , mm ² /s	2.34	7.15
β , $\times 10^{-10}$ Pa ⁻¹	1.34	4.39
ϵ	1.7×10^{-4}	1.7×10^{-4}
$\sigma_n - p_a$, MPa	18	18
ρ , kg/m ³	2800	2800

^aA fuller discussion on the origin of the parameters is included in *Platt et al.* [2014].

by fitting to the experimental data in *Marone et al.* [1990]. As with the frictional parameters, ϵ is inferred from experiments performed at strain rates much lower than those considered here. The value of ϵ appropriate for high strain rates is uncertain.

Some observations of strain localization come from borehole drilling, which typically intersects the fault at a depth much shallower than 7 km [*Heermance et al.*, 2003; *Boullier et al.*, 2009]. To allow comparisons with these observations we also select an additional set of parameters intended to model the uppermost region of the crust, assuming ambient conditions appropriate for a depth of 1 km. These are listed in Table 2, and a full discussion on how these parameters are chosen is included in the companion paper [*Platt et al.*, 2014]. As with the parameters modeling a depth of 7 km, we account for damage to the material using the method in *Rice* [2006]. However, we do not use the path-averaging technique to account for parameter variations due to changes in temperature and pressure, and all parameters are evaluated at the ambient conditions.

The thermal parameters of the problem are more tightly constrained than the hydraulic parameters. We choose the specific heat $\rho c = 2.7$ MPa/K [*Lachenbruch*, 1980; *Mase and Smith*, 1987]. *Rice* [2006] notes a range of 0.5–0.7 mm²/s for α_{th} , and based on this we choose $\alpha_{th} = 0.7$ mm²/s for the nominal parameter sets and take the values from *Rempel and Rice* [2006] for the path-averaged parameter sets.

Current experiments are unable to provide a friction law of the form $f(\dot{\gamma})$ at the high strain rates considered in this study due to the difficulty of isolating the pure frictional response from other temperature and pore fluid-related effects, and problems confining gouge materials at high slip rates. Lacking data in the ideal strain rate range we instead use steady state friction values from low slip rate friction experiments [*Dieterich*, 1979; *Ruina*, 1983; *Tullis and Weeks*, 1986; *Linker and Dieterich*, 1992]. We implicitly ignore dynamic weakening mechanisms such as flash heating [*Rice*, 2006; *Goldsby and Tullis*, 2011] or the as yet poorly understood weakening that seems to be associated with gouge particles in the nanometer size range [*Di Toro et al.*, 2011]. One ad hoc way to account for such a mechanism may be to choose a lower value of f_o . Even when we have accepted the compromise of using the low strain rate friction law to describe seismic deformation, there is still a wide range of possible values for f_o and $(a - b)$. Data from low strain rate experiments on granite under hydrothermal conditions show that both f_o and $a - b$ vary with temperature [*Chester*, 1994; *Blanpied et al.*, 1995, 1998; *Boettcher et al.*, 2007]; another study shows how fault mineralogy can alter the steady state friction coefficient f_o [*Ikari et al.*, 2009]. For the sake of simplicity we will neglect these complications and choose the fixed values $f_o = 0.6$ and $a - b = 0.025$. A strong argument could be made for different values. Predicted thicknesses of shear zones will be shown to be proportional to approximately $(a - b)/f_o^2$, making it straightforward to reinterpret numbers and plots for other choices of the frictional parameters. If a different friction law that depends on strain rate alone is assumed, then effective values of f_o and $a - b$ can be found by linearizing about the uniform strain rate $\dot{\gamma}_o$, as shown in equation (5).

4. Spatially Uniform Solution

In this section we model a homogeneous medium that is uniformly sheared at a constant strain rate $\dot{\gamma} = \dot{\gamma}_o$ under locally undrained and adiabatic conditions, writing the corresponding solutions to equations (9) and (15). The assumption of undrained and adiabatic conditions is valid when the boundaries of the gouge layer are impermeable and thermally insulating. These conditions are also asymptotically valid for the earliest

stage of deformation when diffusion has had very limited time to act. In this scenario the stress, pore pressure, and temperature are independent of y , meaning that

$$\{\tau(y, t), p(y, t), T(y, t)\} = \{\tau_0(t), p_0(t), T_0(t)\} \quad (21)$$

For a gouge layer with a thickness h accommodating a slip rate V , the geometry sketched in Figure 1, *Lachenbruch* [1980] developed an exact solution for this system. The shear stress and pore pressure are related by

$$\tau_0(t) = f_o \bar{\sigma}_0(t) \quad (22)$$

where

$$\bar{\sigma}_0(t) = \sigma_n - p_0(t) = (\sigma_n - p_a) \exp\left[-\frac{f_o \Lambda}{\rho C} \dot{\gamma}_o t\right] \quad (23)$$

where p_a is the ambient pore pressure present before shear begins. This means that

$$\gamma_w = \frac{\rho C}{f_o \Lambda} \quad (24)$$

is the characteristic weakening shear strain for thermal pressurization under undrained and adiabatic conditions. This can be converted to a slip-weakening distance for a gouge layer with a finite thickness h ,

$$D_{ud,ad} = h \frac{\rho C}{f_o \Lambda}. \quad (25)$$

Note that the slip-weakening distance scales with the width of the deforming gouge, making strain localization crucial in the evolution of strength during shear. This will be investigated further in the companion paper [*Platt et al.*, 2014]. *Lachenbruch* [1980] also solved for the temperature evolution

$$T_0(t) = T_0(0) + \frac{\bar{\sigma}_a}{\Lambda} \left[1 - \exp\left(-\frac{f_o \Lambda}{\rho C} \dot{\gamma}_o t\right) \right], \quad (26)$$

where $\bar{\sigma}_a = \sigma_n - p_a$ is the ambient effective stress. Note that our formulation of dilatancy that accounts only for porosity changes due to changes in strain rate does not alter the solution from *Lachenbruch* [1980]. *Lachenbruch* [1980] also considered a constant dilation rate, and in this case the shear strength (22) decays exponentially to a finite value rather than zero. However, if dilation is confined to the early stages of deformation, as is consistent with our formulation of dilatancy, then the effect is essentially to increase $\bar{\sigma}_0(0)$ [see *Rice*, 2006].

For a constant friction coefficient this uniform shear solution is the only possible solution in which the deforming zone has a finite width. The alternative is slip on the plane of maximum pore pressure, with no deformation in the rest of the system. If the rate dependence of the friction law is accounted for, then the straining can localize to a thin zone with a small, but finite, width. In the following section we show what selects this critical width for the deforming zone.

5. Linear Stability of Uniform Shear

In this section we study the stability of small spatial perturbations away from the uniform shear solution. The velocity, pore pressure, and temperature are written as the sum of the spatially uniform solution from the previous section and a small spatially dependent perturbation,

$$\tau(y, t) = f_o \bar{\sigma}_0(t) + \tau_1(y, t) \quad (27a)$$

$$\dot{\gamma}(y, t) = \dot{\gamma}_0 + \dot{\gamma}_1(y, t) \quad (27b)$$

$$p(y, t) = p_0(t) + p_1(y, t) \quad (27c)$$

$$T(y, t) = T_0(t) + T_1(y, t) \quad (27d)$$

where the unperturbed strain rate $\dot{\gamma}_0$ is chosen as the reference strain rate $\dot{\gamma}_0$ in the previous section. Substituting these forms for τ , $\dot{\gamma}$, p , and T into our model from section 2 (equations (1)–(4), (9), and (15)) and linearizing we arrive at

$$\frac{\partial \tau_1}{\partial y} = 0, \quad \tau_1 = (\sigma_n - p_0) \frac{(a-b)}{\dot{\gamma}_0} \dot{\gamma}_1 - f_o p_1 \quad (28a)$$

$$\frac{\partial T_1}{\partial t} = \frac{\dot{\gamma}_0 \tau_1 + f_o \bar{\sigma}_0(t) \dot{\gamma}_1}{\rho c} + \alpha_{th} \frac{\partial^2 T_1}{\partial y^2} \quad (28b)$$

$$\frac{\partial p_1}{\partial t} = \Lambda \frac{\partial T_1}{\partial t} - \frac{\epsilon}{\beta \dot{\gamma}_0} \frac{\partial \dot{\gamma}_1}{\partial t} + \alpha_{hy} \frac{\partial^2 p_1}{\partial y^2} \quad (28c)$$

Next the spatial dependence of the perturbations is decomposed into Fourier modes with wavelength λ ,

$$\{p_1, T_1, \dot{\gamma}_1\} = \Re \left[\{p_1, T_1, \dot{\gamma}_1\}(t) \exp\left(\frac{2\pi i y}{\lambda}\right) \right] \quad (29)$$

where the new functions p_1 , T_1 , and $\dot{\gamma}_1$ now denote complex functions of t alone and $\Re(F)$ indicates the real part of a complex function F . Equations (28a)–(28c) then become

$$\bar{\sigma}_0(t) \frac{(a-b)}{\dot{\gamma}_0} \dot{\gamma}_1 - f_o p_1 = 0 \quad (30a)$$

$$\frac{dT_1}{dt} = \frac{f_o \bar{\sigma}_0(t) \dot{\gamma}_1}{\rho c} - \frac{4\pi^2 \alpha_{th}}{\lambda^2} T_1 \quad (30b)$$

$$\frac{dp_1}{dt} = \Lambda \frac{dT_1}{dt} - \frac{\epsilon}{\beta \dot{\gamma}_0} \frac{d\dot{\gamma}_1}{dt} - \frac{4\pi^2 \alpha_{hy}}{\lambda^2} p_1 \quad (30c)$$

The above equations, a linear but nonautonomous system due to the exponentially decaying $\bar{\sigma}_0(t)$, describe the stability of an unbounded gouge material being sheared uniformly with a strain rate of $\dot{\gamma}_0$. This can be specialized for a gouge layer of thickness h sheared between rigid, impermeable, and thermally insulating blocks moving relative to each other with a slip rate V using the boundary conditions

$$\frac{\partial T}{\partial y} = \frac{\partial p}{\partial y} = 0 \quad \text{at } y = 0, h \quad (31)$$

These can be satisfied by perturbations that are proportional to the Fourier mode,

$$\cos\left(\frac{\pi N y}{h}\right) \quad (32)$$

where N is any positive integer and the wavelength is defined by $\lambda = 2h/N$. We see that N corresponds to the number of half-wavelength oscillations in the gouge layer. Once we have determined the allowed values of λ corresponding to growth or decay of strain rate perturbations, and calling λ_{shr} the longest stable wavelength for which strain rate perturbations do not grow, only shear zones with

$$h < \lambda_{shr}/2 \quad (33)$$

will support stable homogeneous shear.

6. Stabilization by Frictional Rate Strengthening Only

First we consider only the effects of frictional rate-strengthening, neglecting dilatancy by setting $\epsilon = 0$. Using equation (30a) we can relate the perturbations in pore pressure and strain rate,

$$\dot{\gamma}_1 = \frac{f_o \dot{\gamma}_0}{(a-b)\bar{\sigma}_0(t)} p_1, \quad (34)$$

allowing us to eliminate $\dot{\gamma}_1$ from equations (30). We arrive at the pair of equations for p_1 and T_1 ,

$$\frac{dT_1}{dt} = \frac{f_o^2 \dot{\gamma}_0}{(a-b)\rho c} p_1 - \frac{4\pi^2 \alpha_{th}}{\lambda^2} T_1 \quad (35a)$$

$$\frac{dp_1}{dt} = \Lambda \frac{dT_1}{dt} - \frac{4\pi^2 \alpha_{hy}}{\lambda^2} p_1 \quad (35b)$$

Remarkably, this subsystem does not explicitly depend on time. It can be solved by perturbations of pressure and temperature of the form

$$\begin{Bmatrix} p_1(t) \\ T_1(t) \end{Bmatrix} = \begin{Bmatrix} p_1(0) \\ T_1(0) \end{Bmatrix} \exp(st) \quad (36)$$

and equation (34) then provides the solution for the strain rate perturbation,

$$\dot{\gamma}_1(t) = \frac{f_o \dot{\gamma}_o p_1(0)}{(a-b)(\sigma_n - p_a)} \exp \left[\left(s + \frac{f_o \Lambda}{\rho c} \dot{\gamma}_o \right) t \right] \quad (37)$$

This is a rare case where a system of linear differential equations with some time-dependent coefficients has exact solutions in exponential form, albeit with coefficients of t in the exponentials that are different for $\dot{\gamma}_1$ than for p_1 and T_1 . Substituting (36) into (35) yields two linear equations for $p_1(0)$ and $T_1(0)$. Since the equations are homogeneous, a nonzero solution is possible only if the determinant of the coefficients vanishes. This requires that s satisfy

$$\frac{f_o^2 \Lambda}{(a-b)\rho c} \dot{\gamma}_o s = \left(s + \frac{4\pi^2 \alpha_{th}}{\lambda^2} \right) \left(s + \frac{4\pi^2 \alpha_{hy}}{\lambda^2} \right) \quad (38)$$

We can use this equation to determine the stability of uniform shear of a fluid-saturated gouge material. If the real part of the exponential coefficient $s + f_o \Lambda \dot{\gamma}_o / \rho c$ is positive, then the perturbation away from uniform straining grows exponentially in time. This exponential growth is interpreted as strain rate localization. Consequently, the condition that uniform shear be linearly stable is

$$\Re \left(s + \frac{f_o \Lambda}{\rho c} \dot{\gamma}_o \right) < 0 \quad (39)$$

As shown in Appendix A, this condition is equivalent to wavelengths satisfying

$$\lambda < \lambda_{shr} \equiv 2\pi \sqrt{\frac{(a-b)\rho c}{f_o \Lambda} \frac{\alpha_{th} + \alpha_{hy}}{(f_o + 2(a-b))\dot{\gamma}_o}} \quad (40)$$

Spatial perturbations with wavelengths shorter than the critical value will decay exponentially, and those greater than the critical value will grow exponentially. We highlight (40) as the key result of the linear stability analysis. Interested readers can find a much fuller discussion of the possible behaviors associated with different values of s in Appendix A.

6.1. Width of the Localized Zone

We now evaluate the critical wavelength using the nominal parameter set for intact material at a depth of 7 km. For a representative seismic slip rate $V = 1$ m/s accommodated over a gouge thickness $h = 10$ mm, leading to a nominal strain rate $\dot{\gamma}_o = 100$ s⁻¹, the critical wavelength is $\lambda_{shr} = 0.34$ mm. Recall that for a layer of thickness h the largest possible half-wavelength satisfying insulating and impermeable boundary conditions at the edge of the gouge layer is $\lambda/2 = h$. If the strain rate $\dot{\gamma}_o = 100$ s⁻¹, then the critical half wavelength is much less than the layer thickness, and thus, homogeneous shearing is unstable. Straining will not be distributed over the gouge thickness but, as more fully studied in the companion paper [Platt *et al.*, 2014], will localize to a thinner zone within the gouge comparable to the critical half wavelength.

Figure 2 shows the critical half wavelength as a function of the gouge layer width h for each of the four parameter sets and a fixed slip rate of $V = 1$ m/s, representative of the time-averaged slip rate in tectonic earthquakes. This value of V can be compared with the slip rate range 0.48–1.5 m/s found as the ratio of the slips to slip durations inferred for seven earthquakes analyzed in Heaton [1990]. The average slip rate for this range of values is 0.95 m/s. As h increases the strain rate $\dot{\gamma}_o$ decreases leading to wider critical half wavelengths. We note that parameters modeling damaged material predict larger values of $\lambda_{shr}/2$ than the parameter sets modeling an intact material, due to larger values of α_{hy} and lower values of Λ in the damaged parameter sets. The path-averaged parameters predict larger values of $\lambda_{shr}/2$ than the nominal parameter sets, possibly suggesting that $\lambda_{shr}/2$ will increase during shearing.

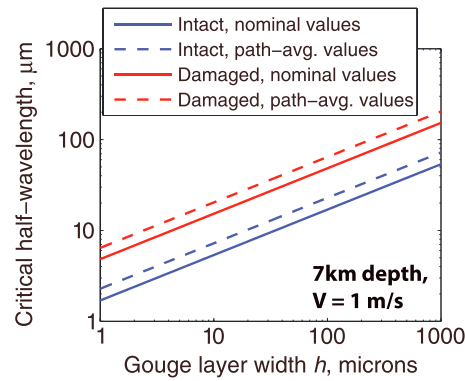


Figure 2. Rate-strengthening friction: A plot showing how the critical half-wavelength $\lambda_{shr}/2$ varies with gouge layer thickness for parameters modeling a depth of 7 km and a slip rate $V = 1$ m/s. Since $\dot{\gamma}_o = V/h$ thicker gouge layers experience lower strain rates, leading to a wider critical half wavelength. Modeling damage as in Rice [2006], we find that damaged material is less susceptible to localization due to larger hydraulic diffusion and less efficient thermal pressurization. When we use the path-averaging method from Rice [2006] to account for parameter variations with pressure and temperature the predictions increase by about a factor of 2.

To turn the critical half wavelength into a consistent estimate for the localized zone thickness W_{rsf} , based on rate-strengthening friction, we search for solutions where the critical half wavelength is equal to the gouge layer thickness by setting,

$$\frac{\lambda_{shr}}{2} = W_{rsf}, \quad \dot{\gamma}_o = \frac{V}{W_{rsf}}, \quad (41)$$

leading to the formula

$$W_{rsf} = \pi^2 \frac{(a-b)\rho c}{f_o \Lambda} \frac{\alpha_{hy} + \alpha_{th}}{V(f_o + 2(a-b))}. \quad (42)$$

Figure 3 shows a graphical solution for this problem. Typical friction data from low strain rate experiments show $f_o \gg (a-b)$, which allows us to simplify the formula to

$$W_{rsf} = \pi^2 \frac{a-b}{f_o^2} \frac{\rho c}{\Lambda} \frac{\alpha_{hy} + \alpha_{th}}{V}. \quad (43)$$

We see that the critical thickness is a balance between competing processes. Fluid and thermal diffusion and rate-dependent frictional strengthening tend to expand the zone, while thermal pressurization tends to narrow it.

Our predictions for the localized zone thickness are equivalent to the widest gouge layer that can be sheared uniformly. Localization is expected to occur when the initial width of the deforming zone is thicker than this critical width, and numerical simulations in Platt *et al.* [2014] show that straining localizes until it reaches a width very similar to the thickness predicted by equation (42). This allows us to compare the predictions from equation (42) with field and laboratory observations of localized shear zones sitting within a broader gouge layer without having to make any assumptions about the initial thickness of the deforming zone.

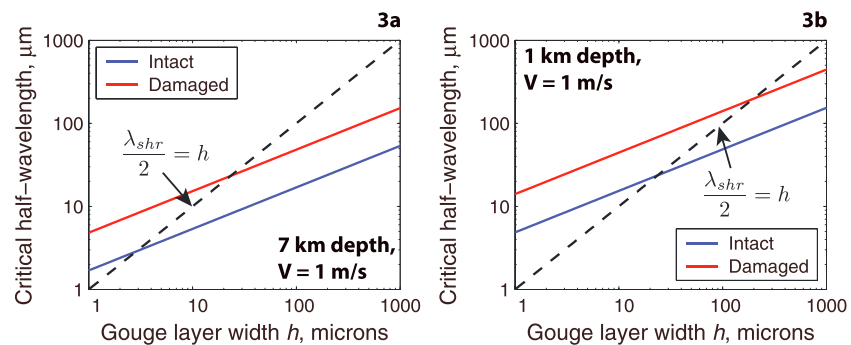


Figure 3. Rate-strengthening friction: A pair of plots showing how the critical width W_{rsf} can be calculated graphically for depths of 1 km and 7 km. Both plots use the nominal parameter sets and a slip rate $V = 1$ m/s. To find the self-consistent width for the shear zone we look for points at which the critical half wavelength is equal to the gouge layer thickness. This condition is indicated by the black line, and the intersection points give the localized zone thickness for the different parameter sets. Localization is expected when the gouge layer thickness is greater than this critical width, and uniform shear is expected when the gouge layer thickness is thinner than this critical width. Using the nominal parameter sets for a depth of 7 km we predict a width of 3 μm for the intact material, and a width of 23 μm for the damaged material. Accounting for changes in the parameters with pressure and temperature using the path-averaging technique of Rice [2006] increases both of these predictions by a factor of 2. At a depth of 1 km we predict a width of 24 μm for the intact material and 197 μm for the damaged material. We do not have access to path-averaged parameter sets for a depth of 1 km, but we tentatively assume that the change in localized zone width due to changes in parameters with pore pressure and temperature will be the same at 1 km and 7 km.

We now evaluate equation (42) for the different parameter sets. For a depth of 7 km, using the superscripts *int* to represent intact material, *dam* to represent damaged material, *n* for nominal parameter sets, and *pa* for path-averaged parameter sets,

$$\begin{aligned} W_{\text{rsf}}^{\text{int},n} &= 3 \mu\text{m} & , & & W_{\text{rsf}}^{\text{int},\text{pa}} &= 5 \mu\text{m}, \\ W_{\text{rsf}}^{\text{dam},n} &= 23 \mu\text{m} & , & & W_{\text{rsf}}^{\text{dam},\text{pa}} &= 41 \mu\text{m}. \end{aligned} \quad (44)$$

Comparison of the nominal and path-averaged parameters demonstrates that variations with pressure and temperature do not strongly influence the results, changing W_{rsf} by about a factor of 2. More important in controlling the width is the amount of damage. Damaged material has a larger value of α_{hy} and a smaller value of Λ , leading to predictions for W_{rsf} that are an order of magnitude wider than those for intact material. Caution must be used in applying this result, since the model for damage used in Rice [2006] is somewhat arbitrary.

Next we compare the predictions for a depths of 7 km and 1 km. Using the parameters from Platt *et al.* [2014] for an ambient effective stress $(\sigma_n - p_a) = 18$ MPa, summarized in Table 2; in (42) we find

$$W_{\text{rsf}}^{1 \text{ km},\text{int}} = 24 \mu\text{m} \quad , \quad W_{\text{rsf}}^{1 \text{ km},\text{dam}} = 197 \mu\text{m}. \quad (45)$$

The localized zone is predicted to be wider at shallower depths. When considering the parameters modeling a depth of 7 km, the path-averaged values approximately doubled W_{rsf} for both intact and damaged material. Although we do not have calculations of path-averaged parameters for a depth of 1 km, we tentatively assume they will also increase W_{rsf} by 70 – 80%, suggesting widths of $\sim 40 \mu\text{m}$ for intact material, and $\sim 350 \mu\text{m}$ for damaged material.

We note that Benallal and Comi [2003] have addressed the possible instability of spatially homogeneous elastic-plastic deformation, and onset of localized straining, in fluid-saturated porous media. That was studied initially without consideration of the effects of frictional heating and thermal pressurization, with those effects being added to their analysis subsequently by Benallal [2005]. Their model did not include a nonzero viscoplastic, or rate dependence, of friction, which is represented here by the $(a - b)$ term and is seen in the expressions above, and in the accompanying paper [Platt *et al.*, 2014], to be critical to our results for a nonzero thickness of the localized zone, which vanishes when $(a - b) \rightarrow 0$.

7. Stabilization by Dilatancy Only

7.1. Transient Growth of Perturbations

Neglecting frictional rate strengthening corresponds to taking $(a - b) \rightarrow 0$ in (30a), which requires that the perturbation in pore fluid pressure vanish. Setting $p_1 = 0$ in equation (30c) we find

$$-\Lambda T_1(t) + (\epsilon/\beta \dot{\gamma}_o) \dot{\gamma}_1(t) = (\epsilon/\beta \dot{\gamma}_o) C \quad (46)$$

where C is the constant

$$C = \dot{\gamma}_1(0) - (\Lambda \beta \dot{\gamma}_o / \epsilon) T_1(0). \quad (47)$$

We can use (46) to eliminate T_1 from (30b) leading to an equation for $\dot{\gamma}_1$ alone. To have a more compact notation in the formulae which follow we redefine the strain rate perturbation $\dot{\gamma}_1$ as a function of the nondimensional time $\hat{t} = t/t_w$, where $t_w = \rho c / f_o \Lambda \dot{\gamma}_o (= \gamma_w / \dot{\gamma}_o)$ is the characteristic weakening time for the homogeneous solution from Lachenbruch [1980] given in equation (23). We arrive at the following equation for $\dot{\gamma}_1(\hat{t})$,

$$\frac{d\dot{\gamma}_1}{d\hat{t}} = \left(\frac{1}{E} \exp(-\hat{t}) - \frac{1}{\hat{\lambda}^2} \right) \dot{\gamma}_1 + \frac{C}{\hat{\lambda}^2}, \quad (48)$$

where E is a dimensionless parameter measuring the strength of the gouge dilatancy,

$$E = \frac{\epsilon}{(\sigma_n - p_a)\beta}, \quad (49)$$

and $\hat{\lambda}$ is the nondimensionalized wavelength,

$$\hat{\lambda} = \lambda / L_{\text{thd}} \quad , \quad L_{\text{thd}} = 2\pi \sqrt{\alpha_{\text{th}} t_w} \quad (50)$$

Here L_{thd} is the length scale over which thermal diffusion acts on a timescale comparable to the weakening timescale t_w . The long time solution of equation (48) is $\dot{\gamma}_1(\hat{t} \rightarrow \infty) = C$, where C is the constant defined in equation (47) and is on the order of the initial perturbations in strain rate and temperature. While strain rate perturbations will always decay, for small values of E the solution can experience rapid initial growth.

If $\dot{\gamma}_1$ is to experience large transient growth before decaying back to C , there must be a point satisfying

$$\frac{d\dot{\gamma}_1}{d\hat{t}} = 0 \quad , \quad \dot{\gamma}_1 \gg C. \quad (51)$$

Equation (48) allows us to calculate that such a turning point must occur at,

$$t_{\text{max}} = t_w \log \left(\frac{\hat{\lambda}^2}{E} \right). \quad (52)$$

From this we conclude that transient growth of $\dot{\gamma}_1$ will only be possible when $t_{\text{max}} > 0$, and thus,

$$\lambda > L_{\text{thd}} \sqrt{E}. \quad (53)$$

Recalling that L_{thd} depends on the nominal strain rate $\dot{\gamma}_o$, this inequality can be converted into a critical gouge layer thickness W_{dil} that must be exceeded for transient localization to be possible. As with the frictional rate strengthening-only case, this is done by setting

$$W_{\text{dil}} = \frac{L_{\text{thd}} \sqrt{E}}{2} \quad , \quad \dot{\gamma}_o = \frac{V}{W_{\text{dil}}}, \quad (54)$$

leading to

$$W_{\text{dil}} = \pi^2 \frac{\rho C \alpha_{\text{th}}}{f_o \Lambda V} \frac{\varepsilon}{\beta \bar{\sigma}_a}. \quad (55)$$

For gouge layers with thicknesses greater than W_{dil} uniform shear will be initially unstable and $\dot{\gamma}_1$ will undergo transient growth.

We now calculate the values of W_{dil} for the different parameter sets modeling a depth of 7 km. We find,

$$\begin{aligned} W_{\text{dil}}^{\text{int},n} &= 0.87 \mu\text{m} \quad , \quad W_{\text{dil}}^{\text{int},pa} = 0.81 \mu\text{m}, \\ W_{\text{dil}}^{\text{dam},n} &= 1.08 \mu\text{m} \quad , \quad W_{\text{dil}}^{\text{dam},pa} = 0.35 \mu\text{m}, \end{aligned} \quad (56)$$

Here we have used the previous superscript definitions to indicate intact or damaged material, and nominal or path-averaged parameters. All four parameter sets predict widths that are on the order of a micron or less. For a given parameter set the values of W_{dil} are at least a factor of 2, and up to a factor of 40, less than the predictions for W_{rsf} . This means that dilatancy, as modeled by *Segall and Rice* [1995], is less effective than frictional rate strengthening at limiting localization for the parameters chosen here. The values of W_{dil} cover a narrower range than the predictions for W_{rsf} .

Next we make a comparison with the parameters for a depth of 1 km. Using the parameters in Table 2, we find

$$W_{\text{dil}}^{1 \text{ km}, \text{int}} = 1.42 \mu\text{m} \quad , \quad W_{\text{dil}}^{1 \text{ km}, \text{dam}} = 1.41 \mu\text{m}, \quad (57)$$

We see that the shallower parameters predict larger values of W_{dil} , but the predictions for W_{dil} at 1 km are still thinner than the smallest prediction for W_{rsf} at 7 km.

While W_{dil} tells us when transient strain rate localization is expected, it does not predict how intense this localization will be when the gouge layer is wider than W_{dil} . To investigate the intensity of localization we solve equation (48) to find the full solution for $\dot{\gamma}_1$,

$$\begin{aligned} \dot{\gamma}_1(\hat{t}) &= \exp \left[\frac{1}{E} \left(1 - \exp(-\hat{t}) \right) - \frac{\hat{t}}{\lambda^2} \right] \\ &\times \left\{ \dot{\gamma}_1(0) + \frac{C}{\lambda^2} \int_0^{\hat{t}} \exp \left[\frac{1}{E} \left(\exp(-\xi) - 1 \right) + \frac{\xi}{\lambda^2} \right] d\xi \right\} \end{aligned} \quad (58)$$

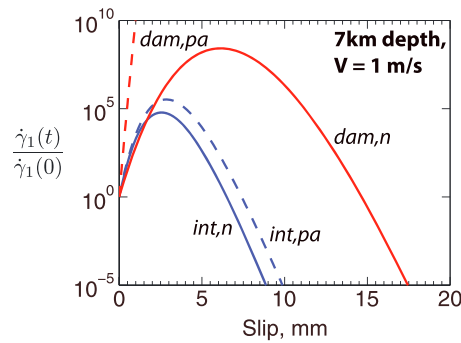


Figure 4. Gouge dilatancy: A plot showing the evolution of the strain rate perturbation $\dot{\gamma}_1$, normalized by the initial value $\dot{\gamma}_1(0)$, for a slip rate of $V = 1$ m/s accommodated across a 1 mm wide gouge layer, a wavelength $\lambda = 100 \mu\text{m}$, and the parameter sets modeling a depth of 7 km (see Table 1). We see dramatic initial growth, followed by a decay back to zero. In our model a damaged material has a higher storage capacity, leading to a smaller value of $E = \epsilon/\beta\sigma_a$, and larger excursions away from homogeneous shearing.

Using the solution for $C = 0$, given in equation (59), we can determine the maximum value of $\dot{\gamma}_1$,

$$\left(\frac{\dot{\gamma}_1(\hat{t})}{\dot{\gamma}_1(0)}\right)_{\max} = \exp\left[\frac{1}{E}\left(1 - \frac{E}{\hat{\lambda}^2}\right) - \frac{1}{\hat{\lambda}^2} \ln\left(\frac{\hat{\lambda}^2}{E}\right)\right], \quad (60)$$

which occurs at $t_{\max} = t_w \log(\hat{\lambda}^2/E)$. As shown in Figure 4 smaller values of E lead to larger peak strain rates, which can be interpreted as more intense localization. Recalling that for $E = 0$ the solution collapses to slip on a plane, we see that as the strength of dilatancy increases the straining is distributed over a wider zone. This fits well with the idea of stabilization by dilatancy.

When calculating this maximum value of $\dot{\gamma}_1$ the assumption that $C = 0$ is valid provided that

$$\dot{\gamma}_1(0) \gg \frac{C}{\hat{\lambda}_2} \int_0^{\log(\hat{\lambda}^2/E)} \exp\left[\frac{1}{E}\left(\exp(-\xi) - 1\right) + \frac{\xi}{\hat{\lambda}^2}\right] d\xi. \quad (61)$$

For small values of E the integrand decays rapidly, and thus, the largest contribution to the integral comes from around $\xi = 0$. This leads us to approximate the integrand as

$$\exp\left[\frac{1}{E}\left(\exp(-\xi) - 1\right) + \frac{\xi}{\hat{\lambda}^2}\right] \approx \exp\left[\left(\frac{1}{\hat{\lambda}^2} - \frac{1}{E}\right)\xi\right]. \quad (62)$$

allowing the integral to be evaluated as

$$\int_0^{t_{\max}} \exp\left[\frac{1}{E}\left(\exp(-\xi) - 1\right) + \frac{\xi}{\hat{\lambda}^2}\right] d\xi \approx \frac{\hat{\lambda}^2 E}{\hat{\lambda}^2 - E}. \quad (63)$$

This approximation is valid to within a few percent when $E < 0.05$. Inequality (61) then simplifies to

$$\dot{\gamma}_1(0) \gg \frac{CE}{\hat{\lambda}^2 - E}. \quad (64)$$

If this condition is not satisfied, then the maximum value of $\dot{\gamma}_1$ given in equation (60) will have an additional contribution which can be calculated using the approximation for the integral developed above. This does not change the conclusion that smaller values of E will lead to larger peak strain rates.

Since the maximum value of $\dot{\gamma}_1$ depends most sensitively on E we calculate values for the different parameter sets. For a the parameter sets modeling a depth of 7 km we find

$$\begin{aligned} E_{\text{int},n} &= 0.0259 & E_{\text{int},pa} &= 0.0245, \\ E_{\text{dam},n} &= 0.0107 & E_{\text{dam},pa} &= 0.0045, \end{aligned} \quad (65)$$

For the case $C = 0$ this has the simple solution,

$$\frac{\dot{\gamma}_1}{\dot{\gamma}_1(0)} = \exp\left[\frac{1}{E}\left(1 - \exp(-\hat{t})\right) - \frac{\hat{t}}{\hat{\lambda}^2}\right]. \quad (59)$$

Figure 4 shows the normalized strain rate perturbation predicted by equation (59) as a function of slip. We observe large initial growth of the perturbations, followed by a return to uniform shearing as the perturbations decay. For a small enough initial perturbation $\dot{\gamma}_1(0)$, the remarkably large $\dot{\gamma}_1(t)/\dot{\gamma}_1(0)$ need not be at conflict with a linearized perturbation approach. However, unless the initial perturbation $\dot{\gamma}_1(0)$ is taken to be unrealistically small, the size of the perturbations far exceeds the region in which the linearized model can be applied. The linearized behavior observed is in qualitative agreement with the numerical simulations for the fully nonlinear system presented in Platt et al. [2014], so we use these linearized results to predict which parameters are most important in controlling the severity of localization.

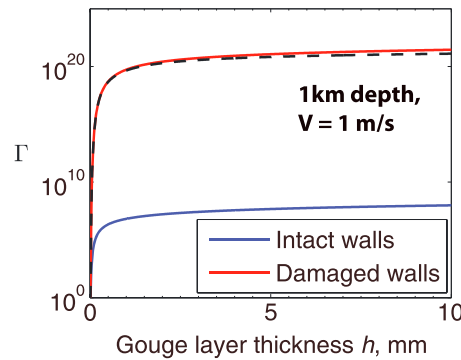


Figure 5. Gouge dilatancy: A plot of the total perturbation strain parameter Γ versus gouge layer thickness for the parameters modeling a depth of 1 km (see Table 2). Damaged material experiences more intense strain localization, in contrast with the results for stabilization by frictional strengthening alone. The dashed line shows the asymptotic approximation from equation (69), which agrees well with the values of Γ found by integrating equation (67) numerically. This linearized analysis is only valid while the perturbations are small compared to the uniform shear solution. For the largest values of Γ this will only be true for unrealistically small values of $\dot{\gamma}_1(0)$. However, we still argue that localization stabilized by dilatancy alone is highly sensitive to changes in E and insensitive to changes in other parameters.

$$\Gamma = \frac{\dot{\gamma}_o \dot{\gamma}_1(t \rightarrow \infty)}{\dot{\gamma}_w \dot{\gamma}_1(0)}. \quad (68)$$

For $E \ll 1$ the integral in equation (67) can be approximated using Laplace's method [Bender and Orszag, 1999] to find

$$\Gamma \sim \hat{\lambda} \sqrt{2\pi} \exp \left[\frac{1}{E} \left(1 - \frac{E}{\hat{\lambda}^2} \right) - \frac{1}{\hat{\lambda}^2} \ln \left(\frac{\hat{\lambda}^2}{E} \right) \right], \quad (69)$$

which for large values of $\hat{\lambda}$ simplifies to

$$\Gamma \sim \hat{\lambda} \sqrt{2\pi} \exp \left(\frac{1}{E} \right). \quad (70)$$

The exponential function means that Γ depends sensitively on E and is relatively insensitive to changes in $\hat{\lambda}$. Setting $\lambda/2 = h$, corresponding to a single localized straining peak located at the boundary of the gouge layer, we now plot Γ as a function of gouge layer thickness for the different parameter sets. As predicted Γ reaches a value relatively independent of h , with this final value largely controlled by the value of E . Larger values of E lead to smaller values of Γ showing that stronger dilatancy will lead to a wider localized zone. The asymptotic approximation (69) is plotted in Figure 5 alongside the actual values of Γ , showing that the asymptotic approximation provides a good prediction for Γ .

As before the assumption that $C = 0$ is valid provided that inequality (64) is satisfied. If this is not true, then there will be an additional prefactor in equation (69), but this does not change the conclusion that Γ depends most sensitively on E .

8. Discussion

8.1. Frictional Rate Strengthening Only

Equation (42) predicts a localized zone thickness W_{rf} as a function of the gouge properties and the slip rate V . The shear zone thickness is set by a balance between thermal pressurization, diffusion, and frictional rate strengthening. Using the parameters from section 3, this formula was used to predict localized zone thicknesses in the range 3–41 μm for a depth of 7 km and a slip rate $V = 1$ m/s. We now discuss how various factors could alter these predictions.

Here we have used the previous superscript definitions to indicate intact or damaged material, and nominal or path-averaged parameters. For a depth of 1 km we find

$$E_{1 \text{ km, int}} = 0.0705, \quad E_{1 \text{ km, dam}} = 0.0215, \quad (66)$$

We see that the shallower parameters have larger values of E , leading us to expect more stabilization from dilatancy at shallower depths, and thus wider localized zones.

7.2. Total Strain Accumulated

Field observations are unable to observe in situ strain rates and can only, at best, observe the final strain distribution. Motivated by this we integrate the strain rate perturbation $\dot{\gamma}_1$ to find the total perturbation strain,

$$\gamma_1(t) = \frac{\dot{\gamma}_w}{\dot{\gamma}_o} \int_0^{\hat{t}} \dot{\gamma}_1(s) ds \quad (67)$$

Taking $\hat{t} \rightarrow \infty$ we capture all of the transient localization, allowing us to define a measure of the total perturbation strain,

While the analysis above considered a fixed slip rate applied across the gouge layer, in reality the slip rate will vary dramatically during seismic slip. Previous dynamic rupture simulations accounting for thermal pressurization showed that slip rates within the slipping patch of the fault vary by at least an order of magnitude, with the largest slip rates near the rupture tip [Noda *et al.*, 2009; Garagash, 2012]. The linear stability analysis predicts $W_{\text{rsf}} \propto 1/V$, suggesting that the localized zone thickness will evolve with V during seismic shear. For the slip rate profiles in Noda *et al.* [2009] and Garagash [2012] the zone of localized zone shear will be thinnest at the rupture tip and will gradually widen as shear continues. Large changes in localized zone thickness during rupture may make it hard to compare our prediction for localized zone thickness with field observations of final strain profiles. We intend to address the variable slip rate scenario in future work.

Next we discuss the influence of the frictional parameters on W_{rsf} . We recall that the linear stability analysis is valid for any rate-strengthening friction law that depends on $\dot{\gamma}$ alone, and for a general friction law the parameter $(a - b)$ is defined as

$$(a - b) = \dot{\gamma}_o \left. \frac{\partial f(\dot{\gamma})}{\partial \dot{\gamma}} \right|_{\dot{\gamma}_o}. \quad (71)$$

Equation (42) provides the framework to discuss how our predictions would change for different friction laws. We see that W_{rsf} scales linearly with $(a - b)$, meaning that a friction law that exhibits stronger rate strengthening will more effectively limit localization leading to wider localized shear zones. Also, $W_{\text{rsf}} \propto f_o^{-2}$, the most sensitive dependence of W_{rsf} on any parameter. If other dynamic weakening mechanisms such as flash heating or nanoscale effects are active, and these mechanisms can be modeled in an ad hoc fashion by reducing f_o without altering $(a - b)$, then we expect dynamic weakening to lead to wider localized zones. A drop from $f_o = 0.6$ to $f_o = 0.2$, a typical friction value from Goldsby and Tullis [2011] and Di Toro *et al.* [2011], would increase the localized zone width by a factor of 9. Precise predictions are hard until laboratory experiments are able to separate strain rate, temperature, and pore fluid effects at high strain rates to provide a function $f(\dot{\gamma})$.

The parameter sets used in this paper use the model for damage proposed in Rice [2006]. In this model the permeability is increased by an order of magnitude and the drained compressibility by a factor of 2. The parameter sets modeling a damaged material predict a localized zone width approximately 5 times wider than those for an intact material. This is because the increased permeability leads to more efficient hydraulic transport, while the increased pore volume compressibility leads to less efficient thermal pressurization, as shown by the values of Λ in Table 1. Other damage models will predict different parameter values, but the generality of the formula for W_{rsf} allows other damage models to be used to predict a localized zone thickness. Any damage that increases the permeability or makes thermal pressurization less efficient will lead to a wider shear zone.

Since the linear stability analysis only has a simple exponential solution when the gouge properties are constant, we accounted for parameter changes due to changes in pore fluid state using the path-averaging approach suggested in Rice [2006]. A better approach is to solve numerically using the full equation of state for the pore fluid and allowing the hydraulic properties of the gouge to vary with effective stress, as done by Rempel and Rice [2006] for a uniformly sheared gouge layer. They found that the most significant parameter variation was the change in permeability due to changes in pore pressure. Using the data from Wibberley and Shimamoto [2003], we see that the gouge may experience an order of magnitude increase in permeability, or possibly more, as the pore pressure goes from the ambient conditions to a pore pressure that is a significant fraction of the compressive stress. Assuming that as observed by Rempel and Rice [2006], the dependence of permeability on pore pressure is the most important change, this suggests that our estimates for W_{rsf} may be an order of magnitude too low. Since the loading and unloading paths differ for the permeability data in Wibberley and Shimamoto [2003], the exact value of the permeability for a given effective stress will also depend on the maximum effective stress the gouge has previously experienced, possibly making the exhumation history of the gouge an important variable to consider when comparing with field observations.

8.2. Dilatancy Only

Our analysis in section 7 showed that for the dilatancy-only system strain rate perturbations always decay as $t \rightarrow \infty$. However, strain rate perturbations can experience initial transient growth whenever the gouge layer thickness exceeds the critical value W_{dil} . This critical thickness is a balance between thermal pressurization,

thermal diffusion, and dilatancy. For the parameter sets modeling a depth of 7 km (see Table 1) we predict values of W_{dil} between 0.35 μm and 1.08 μm . In contrast with the predictions for W_{rsf} , the predictions for W_{dil} do not change dramatically when we change from modeling an intact gouge to a damaged gouge. This is because, for the parameterization for damage given in Rice [2006], the decrease in Λ is balanced by an increase in the storage capacity β . For a given parameter set these values of W_{dil} are at least a factor of 2 thinner than the localized zone thickness predictions for stabilization by frictional rate strengthening alone, implying that dilatancy is less efficient at limiting strain rate localization.

When the gouge layer thickness exceeds W_{dil} the strain rate perturbation will experience transient growth. The scaling developed for Γ , the total strain accumulated by the strain rate perturbation, shows the strongest dependence on the parameter $E = \epsilon / \beta \bar{\sigma}_a$. This means that the parameter ϵ plays a crucial role in limiting localization. The value of ϵ used in section 7 is taken from Segall and Rice [1995], which fitted to the low strain rate experiments in Marone *et al.* [1990]. However, for the high strain rates considered here this value of ϵ may not be appropriate. The sensitive dependence of Γ on ϵ means that even a modest increase in ϵ should lead to a significant increase in localization limiting due to dilatancy.

If we neglect the significant grain size reduction or even amorphization that may be associated with seismic strain rates, then the localized zone thicknesses predicted for the dilatancy-only model—and the thinnest predictions for the frictional rate strengthening-only model—are comparable to a typical grain size in the gouge. This means that our model may not be valid for the very thinnest localized shear zones when the size of individual grains may be an important localization limiter.

One prediction for the localized zone thickness when the size of individual grains is important can be found in Sulem *et al.* [2011], which studied localization in a fluid-saturated material accounting for the motion of individual grains using a Cosserat microstructure. Another prediction that comes from a wide body of research on localization in granular systems suggests setting the localized zone thickness equal to $10\text{--}20d_{50}$, where d_{50} is the grain size such that 50% by weight of the particles have larger size. A discussion of the many experiments and numerical simulations that lead to this prediction can be found in Rice [2006]. Using the grain size distribution for ultracataclasite from the Punchbowl fault presented in Chester *et al.* [2005], Rice [2006] estimated d_{50} fault gouge to be $\sim 1 \mu\text{m}$, which leads to a localized zone thickness of $10\text{--}20 \mu\text{m}$. We emphasize that care must be taken when extrapolating the results of numerical simulations of granular flows to natural fault gouges because of the narrow range of grain sizes, uniform grain shapes, and two-dimensional geometry used in typical simulations.

8.3. Comparison With Observations

Several field studies have shown evidence of 100 micron-scale strain localization, as discussed in section 1 [Chester *et al.*, 2003; Heermance *et al.*, 2003; De Paola *et al.*, 2008]. Our predictions for localized zone thickness are in good agreement with the lower end of these observations. Elsewhere in this section we have highlighted mechanisms that could increase the localized zone thickness, for example, a reduction in f_0 due to flash heating or nanoparticle effects or an increase in permeability due to elevated pore pressures. If one or more of these mechanisms is activated, then our predictions would be in the middle, or even above, the range of observed localized zone thicknesses.

Not all observations of faults show such extreme strain localization. For example, Boullier *et al.* [2009] presented a study of two boreholes drilled in the Chelungpu fault, which hosted the M_w 7.6 Chi-Chi earthquake in 1999, at depths of 1111 m and 1136 m. Since fault drilling programs typically intersect the rupture surface near the top of the seismogenic zone, we compare these observations with our prediction for localized zone thickness at a depth of 1 km, where we predict a range for W_{rsf} of $24\text{--}350 \mu\text{m}$. The gouge layer that Boullier *et al.* [2009] interpreted to be the principal slip zone was observed to be 0.3 cm and 2 cm, considerably wider than our estimates. The discrepancy between our predictions and the observations of centimeter-wide shear zones could be due to poor constraints in our parameters, or evidence of another localization limiting mechanism that is active at shallow depths.

Interestingly, the study by Heermance *et al.* [2003] sampled the Chelungpu fault in a region near to the observations of Boullier *et al.* [2009], though at a depth of approximately 330 m, which is 800 m shallower than the observation in Boullier *et al.* [2009]. They observed a diffuse shear zone in some locations on the fault and evidence of $50\text{--}300$ micron-wide localization in others. This suggests that there may be significant

along-strike variability in localized zone thickness. The widths observed by *Heermance et al.* [2003] for the highly localized shear zones are in excellent agreement with our predictions for $W_{r_{sf}}$ at a depth of 1 km.

Current laboratory experiments studying the frictional behavior of gouge materials at high deformation rates use a rotary shear configuration. We compare our results with the microstructures in *Kitajima et al.* [2010], which are taken from high-velocity friction experiments on fluid-saturated ultracataclasite from the Punchbowl fault. *Kitajima et al.* [2010, Figure 9] show typical microstructural arrangements in a cross section taken perpendicular to the direction of deformation. At the highest slip rates, present at the exterior of the cylindrical sample, a region of highly localized slip forms. They show the highly localized zone in red. We estimate this zone to have a width of approximately 100 μm .

However, the distinct banded structure of the localized zone noted in *Kitajima et al.* [2010] may indicate that the width of the shear zone at any given moment may be much less than 100 μm . This is in general agreement with other observations of strain localization from laboratory, which were discussed in more detail in section 1. *Brantut et al.* [2008] identified a primary slipping zone 1–10 μm wide, while other studies also reported extreme localization at seismic slip rates [*Boutareaud et al.*, 2008; *Mizoguchi et al.*, 2009].

While these observations of localized zone thickness are in good agreement with our predictions from the frictional rate strengthening-only system, care must be taken when making this comparison. Due to difficulties confining gouge at high slip rates most current experiments are performed at modest normal stress of 1 MPa. Since the critical point for water is at $p = 22.06$ MPa and $T = 374^\circ\text{C}$, this modest normal stress means that the pore water may boil at laboratory conditions even though this will not happen at typical seismogenic conditions. The onset of localization in high-velocity friction experiments has been linked to this phase transition [*Boutareaud et al.*, 2008; *Kitajima et al.*, 2010]. Choosing parameter values to model the experiment is also difficult, and it is unlikely that any of our parameter sets modeling depths of 1 and 7 km will accurately represent the hydraulic properties of the gouge used in high-velocity friction experiments. The phase transition and poorly constrained parameters make comparing our predictions with such experimental observations of localization difficult. Recent advances in gouge confinement [*Reches et al.*, 2012; *Smith et al.*, 2013] now make it possible to do experiments at supercritical pore pressure, eliminating the complications associated with the phase transition.

It should be noted that the geometry assumed in our model is different from the typical rotary shear experiment. Though we hope that far from the concentric cylinders that form the lateral boundaries of the sample the deformation can be well approximated by one-dimensional shearing, we cannot rule out the possibility that the localization is largely controlled by the teflon sleeve used to confine the gouge.

9. Conclusions

In this paper we analyzed the stability of uniform shear in a fluid-saturated gouge material. To prevent the collapsing of the straining region to a mathematical plane, we considered two separate stabilizing mechanisms, frictional rate strengthening, and dilatancy. For both mechanisms we used a linear stability analysis to determine if small perturbations away from uniform shear will grow or decay. We interpret growing perturbations as a sign of strain localization.

For frictional rate strengthening alone we solved for the critical wavelength λ_{shr} separating growing and decaying strain rate perturbations. Localization is expected for perturbations with wavelengths exceeding the critical wavelength λ_{shr} . The critical wavelength depends on the uniform strain rate but was converted into a prediction for the localized zone thickness $W_{r_{sf}}$ that depends only on the slip rate V . This localized zone thickness is found to be a balance between frictional rate strengthening, thermal pressurization, and diffusion. Constraining the parameters is difficult, but using the parameters from *Rempel and Rice* [2006] and *Rice* [2006] modeling a depth of 7 km and frictional data from *Blanpied et al.* [1998], we predict localized zone thicknesses between 3 μm and 41 μm .

In the system stabilized by dilatancy alone strain rate perturbations will always decay, making uniform straining stable as $t \rightarrow \infty$. However, perturbations may experience dramatic transient growth, and this transient growth is interpreted as strain localization. The system has a critical gouge layer thickness above which straining will localize. For the parameters modeling a depth of 7 km we predict critical thicknesses between 0.35 μm and 1.08 μm . When transient strain rate localization does occur the peak strain rate perturbation

is largely controlled by a single dimensionless parameter modeling the efficiency of dilatancy, making ϵ a crucial parameter in our model.

This analysis only determines the initial stability of infinitesimally small perturbations away from uniform shear but neglects nonlinear effects that become important as the perturbations grow. The companion paper [Platt et al., 2014] extends this work using numerical solutions for the full set of equations to determine the width of the localized zone at peak localization, and the impact that strain rate localization has on the shear strength evolution and maximum temperature rise.

Appendix A: Possible Responses for Frictional Rate Strengthening Only

Here we present a more detailed discussion of the possible responses for the frictional strengthening only system. Equation (38) relates the growth exponent s for the perturbations to the wavelength λ of the perturbations. This equation can be solved using standard techniques for quadratic equations to find

$$s = \frac{1}{2} \left(zH\dot{\gamma}_o - \frac{4\pi^2}{\lambda^2} (\alpha_{th} + \alpha_{hy}) \right) \pm \frac{\sqrt{D}}{2} \tag{A1}$$

where D is the discriminant of the equation

$$D = \frac{16\pi^4}{\lambda^4} (\alpha_{th} - \alpha_{hy})^2 - \frac{8\pi^2}{\lambda^2} (\alpha_{th} + \alpha_{hy}) zH\dot{\gamma}_o + z^2 H^2 \dot{\gamma}_o^2. \tag{A2}$$

For simplicity we have used the definitions

$$H = \frac{f_o \Lambda}{\rho c}, \quad z = \frac{f_o}{a - b}. \tag{A3}$$

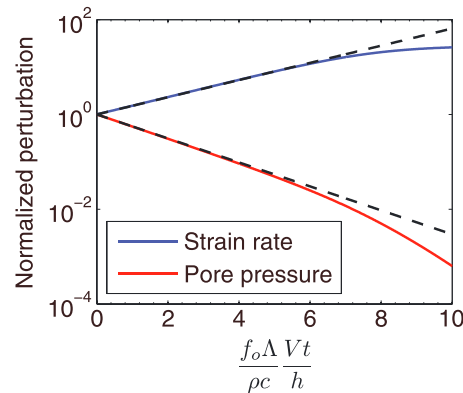


Figure A1. Rate-strengthening friction: A plot showing the normalized perturbations $\dot{\gamma}_1(t)/\dot{\gamma}_1(0)$ and $p_1(t)/p_1(0)$ for the nominal parameters for a damaged material, a uniform strain rate $\dot{\gamma}_o = 1000 \text{ s}^{-1}$, and a perturbation wavelength $\lambda = 310 \text{ }\mu\text{m}$. The linear stability predicts an exponential form for the two perturbations, as shown by the dashed black lines. For the chosen parameters we see that the linear stability analysis predicts that the strain rate perturbation will grow while the pore pressure and temperature perturbations decay. This is supported by the numerical simulations (solid lines) which use the logarithmic friction law as in equation (6), rather than its linearization in equation (4). After the strain rate perturbation has grown sufficiently nonlinear effects become important. We see that the exponential growth predicted by the linear stability analysis does not continue indefinitely, and nonlinear effects limit the strain rate perturbation to a finite value.

Noting that D itself is a quadratic in λ^{-2} , we can solve to find the range for which $D < 0$. When $D < 0$ the exponential coefficient s will have a nonzero imaginary component, signaling an oscillatory response to perturbation with exponentially growing or decaying amplitude. We find that $D < 0$ for the finite range of wavelengths $\lambda_1 < \lambda < \lambda_2$ where,

$$\lambda_1 = 2\pi \frac{|\sqrt{\alpha_{hy}} - \sqrt{\alpha_{th}}|}{\sqrt{zH\dot{\gamma}_o}}, \quad \lambda_2 = 2\pi \frac{\sqrt{\alpha_{hy}} + \sqrt{\alpha_{th}}}{\sqrt{zH\dot{\gamma}_o}}. \tag{A4}$$

Assuming that $D < 0$ when $Re(s) = 0$ we can find the critical wavelength separating growing and decaying perturbations in p and T to be

$$\lambda_{pT} = 2\pi \sqrt{\frac{\alpha_{th} + \alpha_{hy}}{zH\dot{\gamma}_o}}. \tag{A5}$$

For $\lambda > \lambda_{pT}$ perturbations in p and T will grow. Recalling equation (37), which shows that the time dependence for the strain perturbation $\dot{\gamma}_1$ is $s + H\dot{\gamma}_o$, we can determine a similar critical wavelength for the strain rate perturbation $\dot{\gamma}_1$,

$$\lambda_{shr} = 2\pi \sqrt{\frac{\alpha_{th} + \alpha_{hy}}{(z + 2)H\dot{\gamma}_o}}. \tag{A6}$$

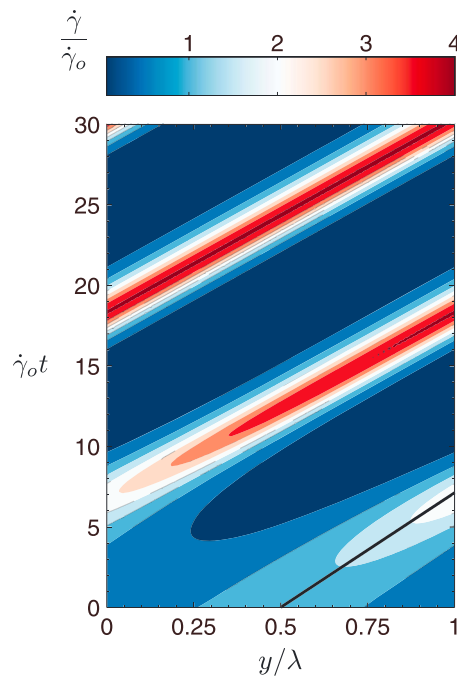


Figure A2. Rate-strengthening friction: A plot showing $\dot{\gamma}(y, t)$ for a system with periodic boundary conditions using the nominal parameters for a damaged material, a uniform strain rate $\dot{\gamma}_0 = 1000 \text{ s}^{-1}$, a perturbation wavelength $\lambda = 360 \text{ }\mu\text{m}$ and an initial pore pressure perturbation that is 1% of the ambient effective stress $\bar{\sigma}_a$. The parameters and uniform strain rate determine the critical wavelength λ_{shr} , and this determines if the perturbation grows or decays. For this case, as predicted by the linear stability analysis, the initial strain rate perturbation propagates as it grows. The black line in the bottom right corner indicates the predicted propagation speed, and we see excellent agreement between the numerical simulations, which are based on the logarithmic friction law in equation (6) and not the linearization given in equation (4), and the analytic prediction. Once nonlinear effects become important, the strain rate perturbation ceases growing but continues to propagate at a speed slightly faster than the predicted phase velocity.

For $\lambda_1 < \lambda < \lambda_2$ there will be an imaginary component to s . This is associated with propagation of the perturbations, with the two complex conjugate roots corresponding to propagation in the positive and negative y direction. This propagation is compatible with a formulation that uses periodic boundary conditions to model an infinite domain, but not with zero flux boundary conditions at the edge of a finite thickness gouge layer. Any propagation of the Fourier mode in the y direction will lead to a perturbation that no longer satisfies the zero flux boundary conditions at the edge of the gouge layer. In the system with zero flux boundary conditions at the boundary of the gouge layer a complex value of s leads to oscillatory growth or decay, provided that the initial conditions are symmetric about the center of the layer this can be thought of as a standing wave. Figure A2 shows $\dot{\gamma}(y, t)$ for a system with periodic boundary conditions using the nominal parameters for a damaged material, a uniform strain rate $\dot{\gamma}_0 = 1000 \text{ s}^{-1}$, and a perturbation wavelength $\lambda = 360 \text{ }\mu\text{m}$. This is based on numerical simulations, again like in Figure A1, but using the logarithmic friction law from equation (6) rather than the linearization given in equation (4). As predicted by the linear stability analysis, we see growth and propagation of the perturbation. The perturbation does not grow indefinitely but is instead capped by nonlinear effects at a finite value. The black line indicates the

For $\lambda > \lambda_{shr}$ the perturbation $\dot{\gamma}_1$ will grow and homogeneous shear is unstable. For all physical parameter choices,

$$\lambda_{shr} < \lambda_{pT} < \lambda_2. \quad (A7)$$

A final ordering $\lambda_1 < \lambda_{shr}$ can also be proven provided that $z > z_c$ where the critical value of z is

$$z_c = \frac{(\sqrt{\alpha_{hy}} - \sqrt{\alpha_{th}})^2}{\sqrt{\alpha_{th}\alpha_{hy}}} \quad (A8)$$

If $z > z_c$ then the assumption $D < 0$ used to calculate the formulas for λ_{pT} and λ_{shr} is true, and the formulae in equations (A5) and (A6) are exactly the critical wavelengths separating growing and decaying perturbations in $\{p, T\}$ and $\dot{\gamma}$, respectively. The four parameter sets considered in this paper lead to the range $z_c = 0.01 - 1.81$, meaning that $z > z_c$ for any realistic values of f_0 and $(a-b)$, which have $f_0 \gg (a-b)$. When $z < z_c$ the formulae for λ_{pT} and λ_{shr} are no longer valid. Noting that the value of α_{th} is relatively well constrained [Rice, 2006], a parameter set with $z < z_c$ would require a value of α_{hy} at least an order of magnitude greater than the largest values assumed here.

Having solved for the critical wavelengths controlling the system we next discuss how perturbations of different wavelengths will evolve. As mentioned before, for $\lambda > \lambda_{pT}$ perturbations in p and T will grow exponentially; similarly for $\lambda > \lambda_{shr}$ perturbations in $\dot{\gamma}$ will grow, making uniform shear of the gouge material unstable. The small difference between λ_{pT} and λ_{shr} means that for a narrow range of wavelengths $\dot{\gamma}_1$ will grow while p_1 and T_1 decay. Figure A1 shows $\dot{\gamma}_1$ and p_1 , normalized by the initial perturbation size, for a system with periodic boundary conditions. This calculation uses the nominal parameters for a damaged material, a uniform strain rate $\dot{\gamma}_0 = 1000 \text{ s}^{-1}$, a perturbation wavelength $\lambda = 310 \text{ }\mu\text{m}$, and the logarithmic friction law in equation (6).

phase velocity predicted by the linear stability analysis, and we see excellent agreement between the predicted propagation speed and that initially observed in the numerical simulations. Once nonlinear effects become important the perturbations continue to propagate, but now do so with a velocity faster than the phase velocity predicted by the linearized analysis.

Acknowledgments

This work was initiated during September 2003 at the Isaac Newton Institute for Mathematical Sciences, University of Cambridge, England, while J.R.R. and J.W.R. were participants in the Program on Granular and Particle Laden Flows but had to be put aside in subsequent years due to other priorities. We are grateful for the support of the Institute and the organizers, and for subsequent support by NSF grants EAR-0809610 and EAR-1315447. This research was supported by the Southern California Earthquake Center. SCEC is funded by NSF Cooperative Agreement EAR-1033462 and USGS Cooperative Agreement G12AC20038. The SCEC contribution number for this paper is 1825. The data used in this paper will be made available online for free.

References

- Beeler, N. M., T. E. Tullis, M. L. Blanpied, and J. D. Weeks (1996), Frictional behavior of large displacement experimental faults, *J. Geophys. Res.*, *101*, 8697–8715.
- Benallal, A. (2005), On localization modes in coupled thermo-hydro-mechanical problems, *C. R. Mécanique*, *333*(7), 557–564, doi:10.1016/j.crme.2005.05.005.
- Benallal, A., and C. Comi (2003), Perturbation growth and localization in fluid-saturated inelastic porous media under quasi-static loadings, *J. Mech. Phys. Solids*, *51*, 851–899, doi:10.1016/S0022-5096(02)00143-6.
- Bender, C. M., and S. A. Orszag (1999), *Advanced Mathematical Methods for Scientists and Engineers: Asymptotic Methods and Perturbation Theory*, Springer, New York.
- Blanpied, M. L., D. A. Lockner, and J. D. Byerlee (1995), Frictional slip of granite at hydrothermal conditions, *J. Geophys. Res.*, *100*, 13,045–13,064.
- Blanpied, M. L., C. J. Marone, D. A. Lockner, J. D. Byerlee, and D. P. King (1998), Quantitative measure of the variation in fault rheology due to fluid-rock interactions, *J. Geophys. Res.*, *103*, 9691–9712.
- Boettcher, M. S., G. Hirth, and B. Evans (2007), Olivine friction at the base of oceanic seismogenic zones, *J. Geophys. Res.*, *112*, B01205, doi:10.1029/2006JB004301.
- Boullier, A.-M., E.-C. Yeh, S. Boutareaud, S.-R. Song, and C.-H. Tsai (2009), Microscale anatomy of the 1999 Chi-Chi earthquake fault zone, *Geochem. Geophys. Geosyst.*, *10*, Q03016, doi:10.1029/2008GC002252.
- Boutareaud, S., D.-G. Calugaru, R. Han, O. Fabbri, K. Mizoguchi, A. Tsutsumi, and T. Shimamoto (2008), Clay-clast aggregates: A new textural evidence for seismic fault sliding?, *Geophys. Res. Lett.*, *35*, L05302, doi:10.1029/2007GL032554.
- Brantut, N., A. Schubnel, J.-N. Rouzaud, F. Brunet, and T. Shimamoto (2008), High-velocity frictional properties of a clay-bearing fault gouge and implications for earthquake mechanics, *J. Geophys. Res.*, *113*, B10401, doi:10.1029/2007JB005551.
- Chester, F. M. (1994), Effects of temperature on friction: Constitutive equations and experiments with quartz gouge, *J. Geophys. Res.*, *99*, 7247–7261.
- Chester, F. M., and J. S. Chester (1998), Ultracataclastic structure and friction processes of the Punchbowl fault, San Andreas System, California, *Tectonophysics*, *295*, 199–221.
- Chester, F. M., J. S. Chester, D. L. Kirschner, S. E. Schulz, and J. P. Evans (2004), Structure of large-displacement, strike-slip faults in the brittle continental crust, in *Rheology and Deformation in the Lithosphere at Continental Margins*, edited by G. D. Kamer et al., pp. 223–260, Columbia Univ. Press, New York.
- Chester, J. S., A. K. Kronenberg, F. M. Chester, and R. N. Guillemette (2003), Characterization of natural slip surfaces relevant to earthquake mechanics, *Eos Trans. AGU*, *84*(46), Fall Meet Suppl., Abstract S42C-0185.
- Chester, J. S., F. M. Chester, and A. K. Kronenberg (2005), Fracture surface energy of the Punchbowl fault, San Andreas System, *Nature*, *437*, 133–136, doi:10.1038/nature03942.
- Coussy, O. (1995), *Mechanics of Porous Continua*, Wiley, New York.
- De Paola, N., C. Collettini, D. R. Faulkner, and F. Trippetta (2008), Fault zone architecture and deformation processes within evaporitic rocks in the upper crust, *Tectonics*, *27*, TC4017, doi:10.1029/2007TC002230.
- Dieterich, J. H. (1979), Modeling of rock friction 1. Experimental results and constitutive equations, *J. Geophys. Res.*, *84*, 2161–2168.
- Di Toro, G., R. Han, T. Hirose, N. De Paola, S. Nielsen, K. Mizoguchi, F. Ferri, M. Cocco, and T. Shimamoto (2011), Fault lubrication during earthquakes, *Nature*, *471*, 494–498, doi:10.1038/nature09838.
- Garagash, D. I. (2012), Seismic and aseismic slip pulses driven by thermal pressurization of pore fluid, *J. Geophys. Res.*, *117*, B04314, doi:10.1029/2011JB008889.
- Garagash, D. I., and J. W. Rudnicki (2003), Shear heating of a fluid-saturated slip-weakening dilatant fault zone 1: Limiting regimes, *J. Geophys. Res.*, *108*, 2121–2139, doi:10.1029/2001JB001653.
- Goldsby, D. L., and T. E. Tullis (2011), Flash heating leads to low frictional strength of crustal rocks at earthquake slip rates, *Science*, *334*, 216–218, doi:10.1126/science.1207902.
- Heaton, T. H. (1990), Evidence for an implications of self-healing pulses of slip in earthquake rupture, *Phys. Earth Planet. Inter.*, *64*, 1–20.
- Heermance, R., Z. K. Shipton, and J. P. Evans (2003), Fault structure control on fault slip and ground motion during the 1999 rupture of the Chelungpu fault, Taiwan, *Bull. Seismol. Soc. Am.*, *93*, 1034–1050.
- Ikari, M. J., D. M. Saffer, and C. J. Marone (2009), Frictional and hydrologic properties of clay-rich fault gouge, *J. Geophys. Res.*, *114*, B05409, doi:10.1029/2008JB006089.
- Kitajima, H., J. S. Chester, F. M. Chester, and T. Shimamoto (2010), High-speed friction of disaggregated ultracataclastic in rotary shear: Characterization of frictional heating, mechanical behavior, and microstructure evolution, *J. Geophys. Res.*, *115*, B08408, doi:10.1029/2009JB007038.
- Lachenbruch, A. H. (1980), Frictional heating, fluid pressure, and the resistance to fault motion, *J. Geophys. Res.*, *85*, 6097–6112.
- Linker, M. F., and J. H. Dieterich (1992), Effects of variable normal stress on rock friction: Observations and constitutive equations, *J. Geophys. Res.*, *97*, 4923–4940.
- Marone, C., C. B. Raleigh, and C. H. Scholz (1990), Frictional behavior and constitutive modeling of simulated fault gouge, *J. Geophys. Res.*, *95*, 7007–7025.
- Mase, C. W., and L. Smith (1985), Pore-fluid pressures and frictional heating on a fault surface, *Pure Appl. Geophys.*, *122*, 583–607.
- Mase, C. W., and L. Smith (1987), Effects of frictional heating on the thermal, hydrologic, and mechanical response of a fault, *J. Geophys. Res.*, *92*, 6249–6272.
- McTigue, D. F. (1986), Thermoelastic response of fluid-saturated porous rock, *J. Geophys. Res.*, *91*, 9533–9542.
- Mizoguchi, K., T. Hirose, T. Shimamoto, and E. Fukuyama (2009), High-velocity frictional behavior and microstructure evolution of fault gouge, obtained from Nojima fault, southwest Japan, *Tectonophysics*, *471*, 285–296, doi:10.1016/j.tecto.2009.02.033.
- Muir-Wood, D. (1990), *Soil Behaviour and Critical State Soil Mechanics*, Cambridge Univ. Press, Cambridge, U. K.
- Noda, H., E. M. Dunham, and J. R. Rice (2009), Earthquake ruptures with thermal weakening and the operation of major faults at low overall stress levels, *J. Geophys. Res.*, *114*, B07302, doi:10.1029/2008JB006143.

- Platt, J. D., J. W. Rudnicki, and J. R. Rice (2014), Stability and localization of rapid shear in fluid-saturated Fault Gouge, 2. Localized zone width and strength evolution, *J. Geophys. Res. Solid Earth*, doi:10.1002/2013JB010711.
- Polissar, P. J., H. M. Savage, and E. E. Brodsky (2011), Extractable organic material in fault zones as a tool to investigate frictional stress, *Earth Planet. Sci. Lett.*, 439–447, doi:10.1016/j.epsl.2011.09.004.
- Reches, Z., and D. A. Lockner (2010), Fault weakening and earthquake instability by powder lubrication, *Nature*, 467, 452–455, doi:10.1038/nature09348.
- Reches, Z., A. S. Madden, and X. Chen (2012), Fault gouge rheology under confined, high-velocity conditions, Abstract T21C-2590 presented at 2012 Fall Meeting, AGU, San Francisco, Calif., 3–7 Dec.
- Rempel, A. W., and J. R. Rice (2006), Thermal pressurization and onset of melting in fault zones, *J. Geophys. Res.*, 111, B09314, doi:10.1029/2006JB004314.
- Rice, J. R. (1999), Flash heating at asperity contacts and rate-dependent friction, *EOS Trans. AGU*, 80(46), Fall Meet. Suppl., F681.
- Rice, J. R. (2006), Heating and weakening of faults during earthquake slip, *J. Geophys. Res.*, 111, B05311, doi:10.1029/2005/JB004006.
- Ruina, A. (1983), Slip instability and state variable friction laws, *J. Geophys. Res.*, 88, 10,359–10,370.
- Schofield, A. N., and P. Wroth (1968), *Critical State Soil Mechanics*, McGraw-Hill, New York.
- Segall, P., and J. R. Rice (1995), Dilatancy, compaction, and slip instability of a fluid-infiltrated fault, *J. Geophys. Res.*, 100, 22,155–22,171.
- Smith, S. A. F., G. Di Toro, S. Kim, J.-H. Ree, S. Nielsen, A. Billi, and R. Spiess (2013), Coseismic recrystallization during shallow earthquake slip, *Geology*, 41, 63–66, doi:10.1130/G33588.1.
- Sulem, J., and V. Famin (2009), Thermal decomposition of carbonates in fault zones: Slip-weakening and temperature-limiting effects, *J. Geophys. Res.*, 114, B03309, doi:10.1029/2008JB006004.
- Sulem, J., I. Stefanou, and E. Veveakis (2011), Stability analysis of undrained adiabatic shearing of a rock layer with Cosserat microstructure, *Granular Matter*, 13, 261–268, doi:10.1007/s10035-010-0244-1.
- Tsutsumi, A., and T. Shimamoto (1997), High-velocity frictional properties of gabbro, *Geophys. Res. Lett.*, 24, 699–702.
- Tullis, T. E., and J. D. Weeks (1986), Constitutive behavior and stability of frictional sliding of granite, *Pure Appl. Geophys.*, 124, 383–414.
- Wibberley, C. A. J., and T. Shimamoto (2003), Internal structure and permeability of major strike-slip fault zones: The Median Tectonic Line in Mie Prefecture, southwest Japan, *J. Struct. Geol.*, 25, 59–78.
- Yund, R. A., M. L. Blanpied, T. E. Tullis, and J. D. Weeks (1990), Amorphous material in high strain experimental faults gouges, *J. Geophys. Res.*, 95, 15,589–15,602.